



# Pattern of vertical velocity in the Lofoten vortex (the Norwegian Sea)

Igor Bashmachnikov<sup>1,2</sup> · Tatyana Belonenko<sup>1</sup> · Pavel Kuibin<sup>3</sup> · Denis Volkov<sup>4,5</sup> · Victor Foux<sup>1</sup>

Received: 21 February 2018 / Accepted: 2 August 2018  
© Springer-Verlag GmbH Germany, part of Springer Nature 2018

## Abstract

Mean radial distributions of various dynamic characteristics of the permanently existing anticyclonic Lofoten vortex (LV) in the Norwegian Sea are obtained from an eddy-permitting regional hydrodynamic MIT general circulation model. It is shown that the model adequately reproduces the observed 3D thermohaline and dynamic structure of the vortex. The obtained radial distribution of the mean vertical velocity is found to form a complex structure: with the upward fluxes along the axis in and above the anticyclonically rotating LV core, compensated by the downward fluxes in the vortex skirt. These vertical motions maintain the vortex potential energy anomaly against dissipation. This secondary circulation is generated by the centrifugal force and, to a lesser extent, by the horizontal dispersion of the vortex energy, both intensified towards the sea surface. Below the vortex core, the maximum downward vertical velocity converges towards the vortex axis with depth. At these depth levels, the secondary circulation is forced by Ekman divergence in the bottom mixed layer. The theory of columnar vortices with helical structure, applied to the LV, relate the radial profiles of the vertical velocity with those of the horizontal circulation. The theoretically predicted the radial patterns of the mean vertical velocity in the LV were close to those, obtained from the primitive equation ocean model, when approximating the radial patterns of the azimuthal velocity with the Rayleigh profile.

**Keywords** Norwegian Sea · Lofoten vortex · Vertical velocity · Divergence · MIT hydrodynamic model · Columnar vortex

## 1 Introduction

An interest of the scientific community to mesoscale vortices of the ocean has been increased during recent decades, as the development of remote sensing technologies and of eddy-permitting numerical models permitted massive statistical

analysis of their properties in the World Ocean (Volkov et al. 2008; Zhmur 2011; Chelton et al. 2007; Chelton et al. 2011). The results of the research have shown that vortices regionally play a significant role in formation of the large-scale distribution of thermohaline properties of ocean waters, exchange of matter through frontal interfaces and affect

---

This article is part of the Topical Collection on the *International Conference “Vortices and coherent structures: from ocean to microfluids”*, Vladivostok, Russia, 28–31 August 2017

---

Responsible Editor: Sergey Prants

---

✉ Igor Bashmachnikov  
igor1969@mail.ru

Tatyana Belonenko  
t.v.belonenko@spbu.ru

Pavel Kuibin  
kuibin@itp.nsc.ru

Denis Volkov  
dlvolkov@gmail.com

Victor Foux  
victorvfl285@yandex.ru

<sup>1</sup> Saint Petersburg State University, 7-9, Universitetskaya nab., Saint Petersburg 199034, Russia

<sup>2</sup> NIERSC- Nansen International Environmental and Remote Sensing Centre, office 49H, 7, 14-th Line V.O., Saint Petersburg 199034, Russia

<sup>3</sup> Kutateladze Institute of Thermophysics, SB RAS, 1 Lavrentyev Ave., Novosibirsk 630090, Russia

<sup>4</sup> Cooperative Institute for Marine and Atmospheric Studies, University of Miami, Miami, FL, USA

<sup>5</sup> NOAA Atlantic Oceanographic and Meteorological Laboratory, Miami, FL, USA

the large-scale ocean dynamics (Maze et al. 1997; Luo and Lu 2000; Golivets and Koshlyakov 2003; Wunsch and Ferrari 2004; Lozier 2010; Bashmachnikov et al. 2015).

Mesoscale vortices, also anticyclonic subsurface lenses, are an important source for increasing biological productivity in many areas of the World ocean (McGillicuddy et al. 2007; Hansen et al. 2010). The increase can be due to a horizontal transfer of nutrients, or to a modification of the depth of the seasonal pycnocline, or to intensified vertical fluxes through the pycnocline in vortex cores (Vaillancourt et al. 2003; Klein and Lapeyre 2009; McGillicuddy et al. 2007; Hansen et al. 2010; Gaube et al. 2013).

Usually mesoscale eddies exist for a relatively short time—a few months (Chelton et al. 2007, 2011; Bashmachnikov et al. 2015). For example, using satellite altimetry, Chelton et al. (2007) obtained an exponential decrease of the number of eddies as a function of their lifetime. Less than 1% of the detected eddies survived for 2 months or more. Long-living eddies travel hundreds and thousands of kilometers through a variable oceanic background which adds uncertainty in studies of their mean properties and dynamics.

The mesoscale Lofoten vortex (LV), quasi-permanently existing in the central part of the Lofoten depression in the Norwegian Sea (68°–72° N and 2° W–10° E), is a rare natural phenomenon. It was first detected during repeated hydrographic cruises of 1970s and 1980s (Alekseev et al. 1991; Romantsev 1991; Ivanov and Korablev 1995a, b; Pereskokov 1999), while latter satellite altimetry observations confirmed that the LV forms a nearly permanent signal (Fig. 1a) with the sea-level anomaly of, on average, 15 cm in the central part of the Lofoten Basin (Kohl 2007; Volkov et al. 2013; Belonenko et al. 2014). The anticyclonic rotation of the LV is detected to extend from the sea surface to the ocean bottom at about 3000 m depth (Bashmachnikov et al. 2017b). However, the LV is not rigidly attached to a distinct feature of bottom topography, as it is usually the case for quasi-permanent mesoscale vortices in the open ocean (White et al. 2007). Not directly interacting with the mean regional currents or steep topography, this anticyclonic vortex presents a “natural laboratory” for a study of decay and re-generation of mesoscale vortices in the ocean.

Even in the background of abnormally warm and salty Atlantic water reservoir of the Nordic Seas, the LV represents a lens with a positive temperature-salinity anomalies at the core depth levels between 300 and 1000 m and with the diameter of 80–100 km (Ivanov and Korablev 1995a; Volkov et al. 2013, 2015; Bashmachnikov et al. 2017b).

A number of recent studies has been exploring horizontal and vertical structure of the LV, as well as explaining the phenomenon of its high stability (Kohl 2007; Raj et al. 2015; Volkov et al. 2015; Bashmachnikov et al. 2017b). In particular, field observations, as well as results of hydrodynamic simulations with Massachusetts Institute of Technology primitive equation general circulation model (MIT GCM), suggest that differential winter convection and the merger with other mesoscale anticyclons are the two main

mechanisms for maintaining the LV against dissipative processes (Kohl 2007; Volkov et al. 2015; Bashmachnikov et al. 2017b). The mesoscale vortices in the basin, some of which eventually serve for re-generation of the LV, are mostly generated as a result of the baroclinic instability of the Norwegian Current near the Lofoten Islands (Kohl 2007; Isachsen 2015).

In this paper, we focus on an almost unexplored subject of the spatial pattern of the vertical velocity in the LV. Being a consequence of non-geostrophic processes in ocean vortices and linked to the processes of their decay, these results will serve for better understanding of temporal evolution of mesoscale vortices in the ocean. The structure of this secondary circulation in the ocean vortices is typically difficult to derive from comparatively short time-series, as the relatively small vertical velocities associated with this circulation are masked by the stronger vertical motions generated by vortex dynamic instabilities or vortex (elliptic) deformations. For in situ or model studies, we typically observe such deformations, the most often characterized by two positive and two negative anomalies in relative vorticity and by the associated upward and downward vertical velocities (Mahdinia et al. 2016; Bashmachnikov et al. 2017b; Pilo et al. 2018). The vertical velocity patterns of the secondary circulation are mostly known for quasi-stationary vortices over seamounts (Mullineaux and Mills 1997; White et al. 2007; Lavelle 2006). In this study, we take advantage of the 12-year long eddy-permitting regional MIT GCM simulations to explicitly derive the mean vertical velocity pattern for a subsurface anticyclonic vortex not attached to a pronounced topographic bump. Further, we compare the velocity structure, obtained from the model, with that predicted by the theory for vortices with a helical structure of threads of relative vorticity (Kuibin and Okulov 1996; Alekseenko et al. 1999).

## 2 Data

We used the same configuration of the MIT GCM as in Volkov et al. (2015) or Bashmachnikov et al. (2017b), the model results provided by Cooperative Institute for Marine and Atmospheric Studies University of Miami NOAA/AOML/PHOD. The horizontal resolution of the model is about  $4 \times 4$  km in the Nordic Seas. The model has 50 geopotential vertical layers; the layer thicknesses vary from 10 m in the upper ocean to 456 m below 3000 m depth. The boundary conditions are taken from the global MIT-ECCO2 model (Estimating the Circulation and Climate of the Ocean, Phase 2),<sup>1</sup> and the initial conditions are based on World Ocean Atlas 2009. The both MIT models use Japanese Re-Analysis (JRA25) for atmospheric forcing. Tested against in situ data, MIT GCM has been proved to fit well the observed structure

<sup>1</sup> <http://ecco2.jpl.nasa.gov>

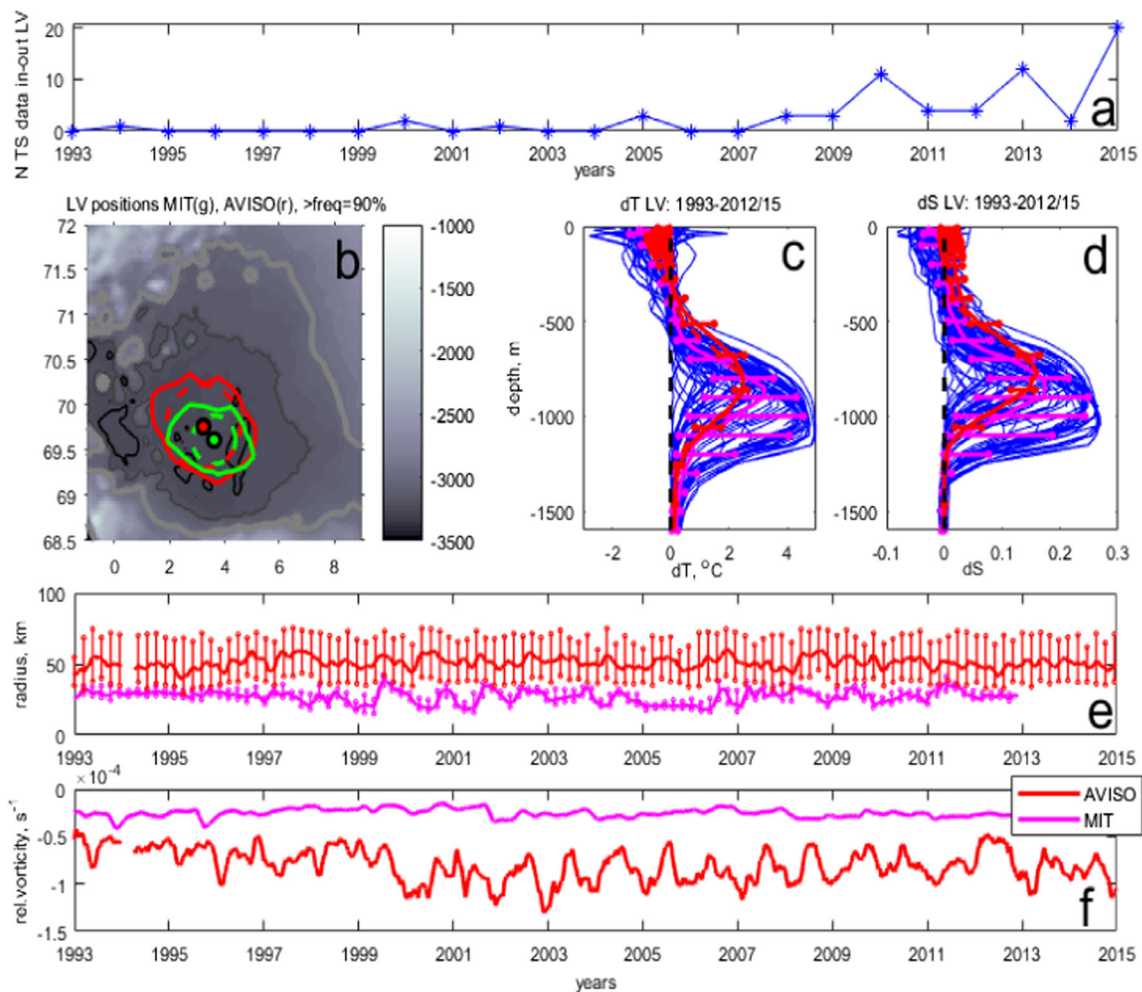


**Fig. 1** Parameters of the LV from MIT GCM and observations. **a** Number of cases per year, when temperature-salinity anomalies were computed, using vertical profiles from EN4 data base (see panels (c) and (d)). **b** Mean positions of the LV center (a color dot), mean LV radius (dashed line), and the isoline (solid lines) limiting the area, within which the LV center was observed 90% of the time of observations; green—MIT GCM, red—AVISO altimetry. The bottom topography (m) is shown in color; isobaths of 2000 m (thick light gray line), 3000 m (thing dark

gray line) and 3250 m (solid black line) are marked. **c, d** Vertical profiles of temperature anomalies (c) and salinity anomalies (d) in the LV core versus the background (blue lines), EN4 data-set. Mean profiles of the anomalies  $\pm$  STD derived from in situ (magenta) and from MIT GCM results (red) are presented. **e** Time evolution of the LV radius (km)  $\pm$  STD from AVISO (red) and MIT GCM (magenta). **f** Time evolution of the LV peak relative vorticity (s<sup>-1</sup>) from AVISO (red) and MIT GCM (magenta)

and dynamics of the Atlantic Water in the Lofoten Basin (Nguyen et al. 2011; Raj et al. 2015; Volkov et al. 2015).

The improved altimetry data-set AVISO14 (<https://www.aviso.altimetry.fr/en/my-aviso.html>) with the horizontal resolution  $0.25^\circ \times 0.25^\circ$  ( $28 \times 10$  km in the Lofoten Basin), covering time period from 1993 to 2015 is used in this study. It has been shown that the new data-set, in particular, permitted to improve eddy detection capabilities: the number of detected eddies using AVISO14 increased as compared to the previous AVISO versions (Capet et al. 2014). When estimating current velocity and relative vorticity from the sea-level data, the noise was minimized by using the 7-point stencil width formulae (Arbic et al. 2012). Applicability of the AVISO altimetry data-set for detection of the LV center and its excursions has been demonstrated by Soiland et al. (2016),

who combined AVISO data-set with an analysis of the trajectory of a RAFOS float, trapped in the LV during 9 months.

Further in this section, we give an outline of the main features of the algorithm for derivation of the LV position, radii and trajectory using AVISO and MIT data-sets (see Bashmachnikov et al. 2017b for details). For LV tracking, horizontal distributions of relative vorticity at a fixed depth level are used. Initially (1st of January 1993), as the first guess, the center of a pronounced negative relative vorticity anomaly in the central part of the Lofoten Basin is selected as the LV center. Starting from the first guess, the position of the LV center within the patch of negative relative vorticity is refined using a set of relative vorticity profiles along several rays, originating in the center of the first guess and covering a circle with the  $30^\circ$  increments. The “edge” of the selected patch of

negative relative vorticity is then defined as the minimum distance from the LV center to a point along a ray where either (1) the relative vorticity profile crosses zero, or (2) the relative vorticity profile forms a local maximum, or else (3) the rate of decrease of the relative vorticity slows down significantly (below 25% of its maximum rate along the initial segment of the ray). The latter two criteria helped detecting the LV boundary even when the LV core is connected by a bridge of negative relative vorticity with another anticyclone or a filament. Second, the LV center is recomputed as the “center of mass” of the obtained edge contour. Then, the procedure is repeated for the refined center position. After three iterations, the final position of the LV center is obtained. The LV radius, under an assumption of the axisymmetric LV, is computed as the mean distance from the LV center to the edge contour. Additionally, the semi-major and the semi-minor axis of an ellipse, fitted to the edge contour, present the maximum and minimum radii, under an assumption of the elliptic LV. At the following field of relative vorticity, the same procedure is repeated, taking the previous position of the LV center as the first guess. Visual inspection showed that the algorithm is very robust and does not allow jumping to a neighboring anticyclonic structure, even when they are stronger than the LV surface signature. During 24 years of LV tracking (1236 time steps), only two artificial corrections of the LV positions in AVISO altimetry had to be done (one in 1994 and another one in 1996). Both algorithm failures occurred when the LV signal in altimetry became very weak and split between two closely connected anticyclonic structures. Visual inspection of these situations suggests that they may represent events of splitting of the LV into two vortices during the eddy interaction with two strong cyclones. When applying the algorithm to the MIT GCM results, no algorithm failures were detected.

For detection of the vertical thermohaline structure of the LV, in situ vertical temperature and salinity profiles were downloaded from EN4 Hadley Center data base (<https://www.metoffice.gov.uk/hadobs/en4/>). The EN4 profiles pass more rigorous quality control procedures and better procedures for removal of duplicate profiles than in the alternative World Ocean Data-base 2013 (<https://www.nodc.noaa.gov/OC5/indprod.html>) (Good et al. 2013). The vertical profiles, that were within the distance of less than 0.75 times the LV radius from the LV center (detected from altimetry), were considered to represent the thermohaline properties of the LV core, while those at distances from 1.2–1.5 times LV radius were taken as the background profiles. To avoid using profiles in strong neighboring cyclones or anticyclones around the LV as the background, the profiles within absolute values of relative vorticity anomalies stronger than  $2 \cdot 10^{-5} \text{ s}^{-1}$  around the LV were not considered. The difference of the thermohaline properties in and outside the LV core at the same depth levels was taken as the LV induced anomalies. From 1236 weeks of the LV tracking, the LV thermohaline

anomalies were obtained during 100 weeks. Ninety percent of the results were obtained after 2008, during the period of a regular sampling of the Lofoten basin by Argo profiling floats (Fig. 1a).

## 3 Results

### 3.1 Vertical and horizontal structure of thermohaline and dynamic properties of the Lofoten vortex from in situ data and model results

The high-resolution version of MIT GCM, used here, has been tested against observations in several previous studies (Kohl 2007; Volkov et al. 2015; Belonenko et al. 2017; Bashmachnikov et al. 2017b). The results showed that the model is able to realistically reproduce water structure and dynamics of the Lofoten Basin, as well as of the LV itself. The main mechanisms responsible for the permanence of the LV in the basin (deep winter convection in the LV core and merger with other anticyclones) are also reproduced by the model. Here, we extend the previous MIT validations, using satellite and in situ observations, to show that the model also reproduces the details of the 3D thermohaline and dynamic structure of the LV.

The results of our automatic tracking procedure (see Section 2) in MIT GCM and in AVISO altimetry data are consistent with the results by Kohl (2007) and by Raj et al. (2015), respectively (Fig. 1b). The frequency of the LV center positioned in each of the grid cells of the study region provide similar results in MIT GCM and in AVISO data. In both data-sets, the LV is typically found in a quite limited area of the Lofoten basin: 70% of time the LV center is found within the distance of the mean LV radius from its mean position, 90% of time—within the distance of 1.5–2 LV radii. Consistent with Kohl (2007), Volkov et al. (2015), and Raj et al. (2015), the data-sets show the dominating cyclonic propagation of the LV within the basin. However, the LV excursions are more confined to the center of the basin in MIT GCM than in AVISO.

For mesoscale eddies, the mean radial profiles of the azimuthal velocity and of the relative vorticity are often close to those of the Rayleigh vortex (Carton 2001). For such vortex, the ratio of the radial distance, at which core the azimuthal velocity reaches its maximum ( $V_{\varphi, \text{max}}$ ), to the radial distance, where the relative vorticity ( $\omega$ ) changes sign, is:  $r(\omega = 0) / r(V_{\varphi, \text{max}}) = \sqrt{2}$  (Bashmachnikov et al. 2017a). The LV dynamic radius (distance from the LV center, where relative vorticity crosses zero) in MIT GCM is  $27 \pm 5$  km (Fig. 1e), while the azimuthal velocity reaches maximum at 18–20 km from the vortex center. This is consistent with the Rayleigh radial profile of the azimuthal velocity. Perfectly matching with MIT GCM results, in situ CTD, ADCP and glider

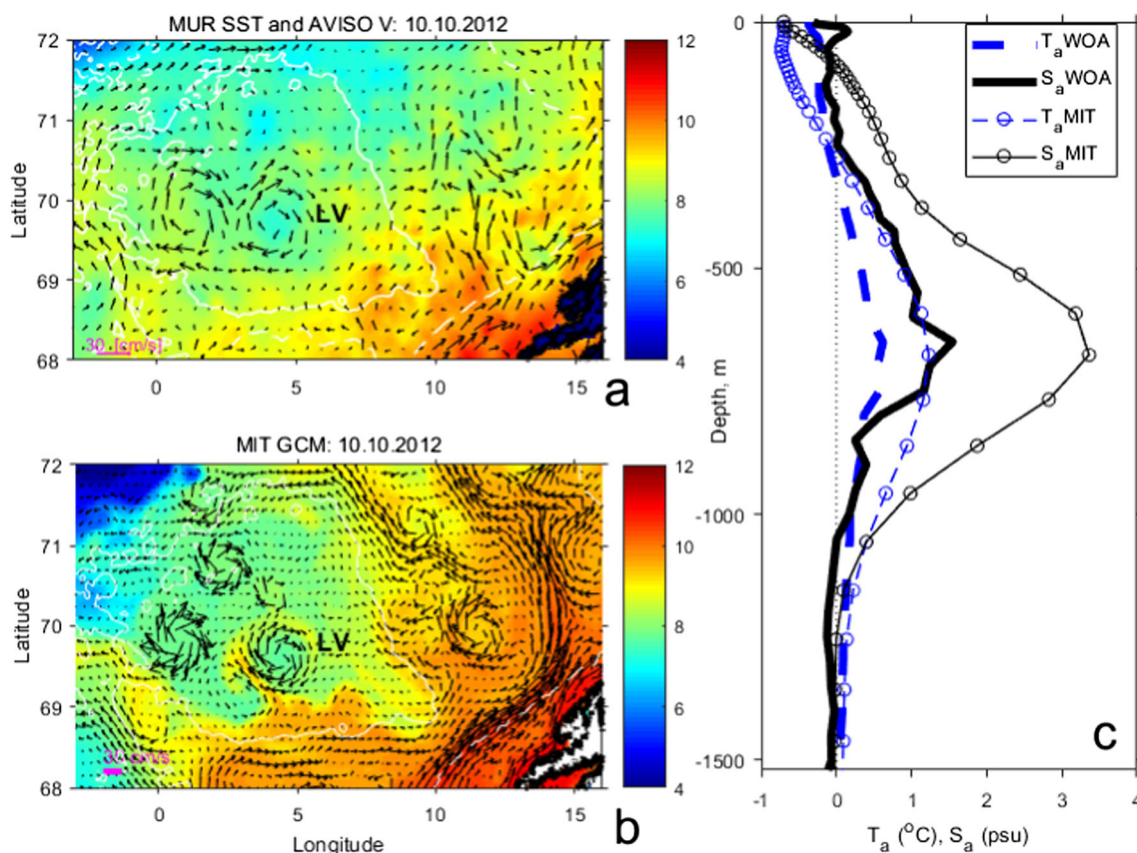


**Fig. 2** **a** Sea surface temperature from MUR data-set (color, °C) and AVISO satellite altimetry currents (vectors) in the Lofoten basin at 10.10.2012. **b** Sea surface temperature (color, °C) and current velocity (vectors, only every third vector is presented) in the Lofoten basin from MIT GCM at 10.10.2012. **c** Vertical profiles of the mean temperature anomalies (dashed blue lines) and salinity anomalies (solid black lines)

surveys show the LV dynamic radius of 24–35 km, while the maximum velocity is reached at 17–20 km from the vortex center (Ivanov and Korabev 1995a, b; Søiland and Rossby 2013; Søiland et al. 2016; Yu et al. 2017). In AVISO data-set, the LV dynamic radius is on average  $50 \pm 10$  km (Fig. 1e), nearly double of that in MIT GCM. Bigger LV radii in AVISO altimetry is a result of at least six times lower horizontal resolution of AVISO data-set, as compared to MIT GCM, as well as of a space-time smoothing during processing and gridding of the sea-level anomalies. However, correctly reproducing the LV size, MIT GCM underestimates the maximum azimuthal velocity of the LV, giving  $30\text{--}50$   $\text{cm s}^{-1}$  in MIT GCM versus  $50\text{--}80$   $\text{cm s}^{-1}$  observed in situ (Søiland and Rossby 2013; Søiland et al. 2016; Yu et al. 2017). The peak relative vorticity of the LV core is also lower: from  $-0.2$  to  $-0.3 \cdot 10^{-4} \text{ s}^{-1}$  in MIT GCM (Fig. 1f, see also Volkov et al. 2015; Bashmachnikov et al. 2017b) versus  $-0.8 \cdot 10^{-4} \text{ s}^{-1}$  observed in situ (Søiland and Rossby 2013; Søiland et al. 2016; Yu et al. 2017) or in AVISO altimetry (Fig. 1f). These model underestimates may be due to a limited model resolution. The effect of the MIT GCM resolution on the LV has been investigated by

inside the LV relative to the surrounding ocean: from the World Ocean Atlas 2013 (thick lines) and MIT GCM (thin lines with circles) averaged from 1993 to 2012. For visibility, the scale for salinity anomalies is multiplied by 50 (the maximum salinity anomaly in the LV, derived from MIT GCM is 0.07)

Volkov et al. (2015). It has been found that the 4-km resolution reasonably well reproduces the amplitude and the size of the eddy kinetic energy anomaly, formed by the LV, when compared to satellite altimetry results. However, the model apparently smooths out some details of the radial structure of the dynamic characteristics in the LV at their peak values.

The in situ vertical profiles of the azimuthal velocity in the LV, derived from CTD observations (Ivanov and Korabev 1995a, b), ADCP observations (Søiland et al. 2016), as well as glider observations (Yu et al. 2017), are closely reproduced by MIT GCM. The simulated azimuthal velocity (and relative vorticity) in the LV slightly increases from the sea surface down to its maximum between 500 and 1000 m. Further down, at 1200–1500 m depths, the mean values of both characteristics rapidly fall to the 1/4–1/5 of their maxima at the eddy core level (Bashmachnikov et al. 2017b).

MIT GCM also well reproduces the observed vertical structure of thermohaline anomalies in the LV (Fig. 1c, d, see also Volkov et al. 2015; Bashmachnikov et al. 2017). The anticyclonic vortex core manifests itself as a positive anomaly of temperature and salinity between 100–200 m and 800–

1200 m depth, well consistent with observations by Alekseev et al. (1991), Ivanov and Korabev (1995a, b), Søiland and Rossby (2013), Yu et al. (2017).

Importantly, in situ data, as well as MIT GCM simulations, show that, on average, the LV forms a negative temperature and salinity anomaly from 200 m depth up, increasing towards the sea surface (Fig. 1c, d). This means that the sea surface temperature (SST) in the center of the anticyclonic LV typically should be lower than at the LV periphery. As an example, Fig. 2a presents two snapshots of horizontal structure of satellite SST from the Multi-Scale Ultra-High Resolution SST (MUR SST, <https://mur.jpl.nasa.gov/>) and surface currents from AVISO altimetry. Figure 2b presents the results of MIT GCM for the same date in October 2012. The snapshots show a close correspondence between the satellite derived structure of the horizontal velocity, the shape and the size of the LV, as well as of other vortices in the basin, and the results of MIT GCM simulations (when comparing figures, one should account for the six times lower resolution of the altimetry maps as compared to the MIT simulations). Here, we stress that the model well reproduces the sea surface negative temperature anomaly over the center of the LV, relative the vortex periphery (see also Raj et al. 2015).

Being practically stagnant and appearing in the time-averaged current velocity fields of the Lofoten basin (in the satellite altimetry, as well as in MIT GCM) as a compact mesoscale anticyclonic structure (Volkov et al. 2015; Raj et al. 2015; Bashmachnikov 2017), the LV core also appears in climatology as a compact positive thermohaline anomaly. The

time-averaged vertical profiles of temperature and salinity anomalies of the LV core, compared to the surrounding waters of the Lofoten Basin, obtained from the World Ocean Atlas 2013 (<https://www.nodc.noaa.gov/OC5/woa13/>) and from MIT GCM simulations, reproduce positive temperature and salinity anomalies at 300–1200 m depth and negative temperature-salinity anomalies above (Fig. 2c, see also Fig. 1c, d). Somewhat lower mean temperature and salinity anomalies in the climatology should be attributed to a stronger blurring of the LV vertical structure from sparse and episodic in situ observations (compare with Fig. 1c, d).

The negative sea surface temperature anomalies over the anticyclonic LV are not surprising. They are often observed over subsurface anticyclones (Bashmachnikov et al. 2013a; Ciani et al. 2017; Barcelo-Llull et al. 2017). The anomalies can be formed by doming of isopycnals over the eddy core (Mullineaux and Mills 1997; White et al. 2007), being a sign of the vortex secondary circulation, as well as by a differential advection of the surrounding water, trapped by an eddy (Bashmachnikov et al. 2013a). This high similarity in the vertical and in the horizontal thermohaline and dynamic patterns of the LV in in situ/satellite data and in the MIT GCM simulations permits us assuming that the model also adequately reproduces patterns of the vertical velocity in the vortex.

Snapshot distributions of the relative vorticity and of the vertical velocity in the LV, derived from MIT GCM (Fig. 3), show intensive dynamic perturbations along the LV boundary of the second azimuthal mode (2 maxima and 2 minima). The perturbations are propagating along the LV boundary at about

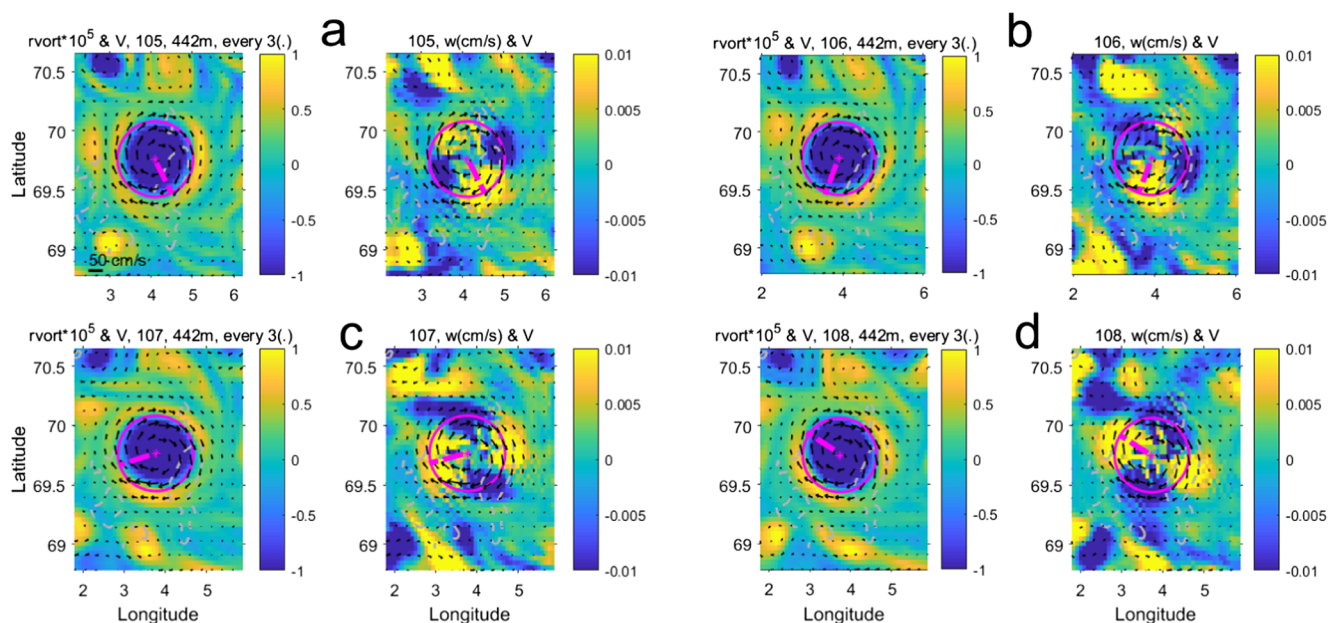


**Fig. 3** Typical patterns of relative vorticity ( $\times 10^{-5} \text{ s}^{-1}$ , left panels) and vertical velocity ( $\text{m s}^{-1}$ , right panels) in MIT GCM at 450 m depth for four consecutive time steps ((a) to (d)) with the time increment of 3 days. Magenta star and magenta circle mark the LV center and the dynamic

radius, respectively. The magenta dashed segment (starting in the LV center) shows, from one panel to another, rotation of the perturbations at the LV boundary

1/3 of the maximum azimuthal velocity of the LV, consistent with the propagation of the second azimuthal mode, generated by baroclinic instability in a vortex (Paldor 1999). The dominance of the second to fourth azimuthal instability modes in the LV has been discussed by Bashmachnikov et al. (2017b) and is consistent with very high-resolution simulations of ocean vortices with similar Rossby and Burger numbers (Mahdinia et al. 2016). When removing the background field of relative vorticity, invoked by the nearly axisymmetric LV, the higher and the smaller values of the overall positive relative vorticity in the LV skirt (left panels in Fig. 3) become positive and negative anomalies. Such anomalies are typical for wave-like dynamic instability patterns in a vortex (Mahdinia et al. 2016). The maxima and minima of vertical velocity (right panels in Fig. 3) fall in-between the maxima and minima of relative vorticity, typical for a progressive wave pattern. Therefore, besides consistency of the mean characteristics of the LV in MIT GCM, we also state consistency of the vertical

velocity patterns in dynamic perturbations at the LV boundary. This gives evidence that MIT GCM adequately reproduces vertical velocity patterns at scales of the LV and even smaller.

Figure 3 also shows that the mean field of vertical velocity of the vortex is largely hidden by much stronger dynamic perturbations of smaller scale. This makes it difficult to derive the mean fields of the vertical velocity even for realistic model studies of ocean eddies. However, the LV presents a rare example of a permanently existing mesoscale vortex structure, making this goal achievable.

### 3.2 The mean radial structure of dynamic parameters of the Lofoten vortex

To separate the mean patterns of the vertical velocity in the LV from the perturbations, in further analysis, we consider the cylinder coordinate system always co-centered with the LV. The radial patterns of LV dynamic parameters at a fixed depth

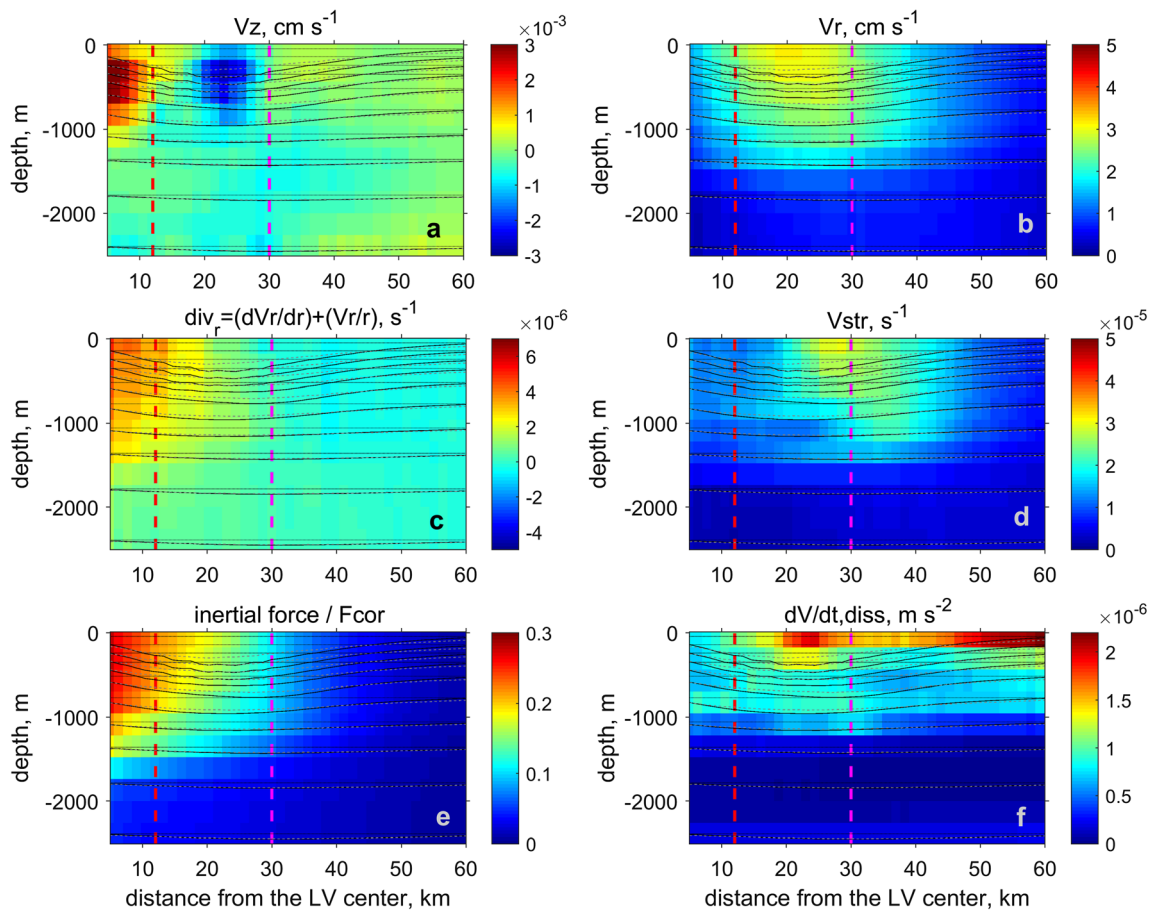


**Fig. 4** Radial distribution of time-averaged characteristics in the LV in MIT GCM, averaged over the model run, as a function of distance from the LV axis: **(a)** the vertical velocity (positive-upward,  $\text{cm s}^{-1}$ ), **(b)** the radial velocity (positive-outwards,  $\text{cm s}^{-1}$ ), **(c)** the radial divergence (positive-outwards,  $\text{s}^{-1}$ , see Eq. 1), **(d)** the horizontal shear stresses ( $\text{s}^{-1}$ ), **(e)** the ratio of the centrifugal force to the Coriolis force, **(f)** variation of the horizontal velocity due to energy dissipation ( $\text{m s}^{-2}$ ). The radial

distributions of the azimuthal velocity (black solid lines) and of the radial velocity (gray dashed lines) for different vertical levels (out of scale) are given with a vertical offset to become zero at the corresponding depth level (see the dotted horizontal zero-velocity lines). Red and magenta vertical dashed lines mark distances of 12 km (depth-mean vertical velocity at the LV core crosses zero) and of 30 km (depth-mean relative vorticity at the LV core crosses zero), respectively

level are obtained by taking averages over the azimuthal coordinate and over the period of simulations. Figure 4 presents such  $r$ - $z$  distributions of various dynamic characteristics of LV derived from MIT GCM. The maximum azimuthal velocity ( $V_{\varphi, \max}$ ) is 20 km from the LV center (see black isolines in Fig. 4) and distance, at which the relative vorticity ( $\omega$ ) changes its sign, is at 30 km from the LV center. The latter distance,  $r(\omega = 0)$ , further in this paper is taken as the characteristic horizontal scale of the vortex ( $\varepsilon$ ).

The time-averaged  $r$ - $z$  distribution of the vertical velocity has a complex structure (Fig. 4a), indicating the presence of a divergence in the upper and in the lower parts of the vortex. This has not previously been demonstrated neither in situ, nor in model studies of mesoscale ocean vortices. The upward vertical velocity in the central part of the LV core and above explains the observed negative temperature (salinity) anomalies above the vortex core (as observed in Figs. 1 and 2). At depth levels from 0 to 1000 m, the radially integrated upward flux in the central core is roughly compensated by the radially integrated downward flux in the vortex skirt (12–30 km from the LV center, e.g., between the red and the magenta lines in Fig. 4a). This asserts consistency of the obtained patterns of the vertical velocity.

In the lower part of the LV core (1200–1300 m), the downward flux in the LV skirt is already about 20% stronger than the upward flux along the vortex axis at the same levels. This assures the overall downward flux at those levels. Below 1500–2000 m only downward vertical velocity is detected.

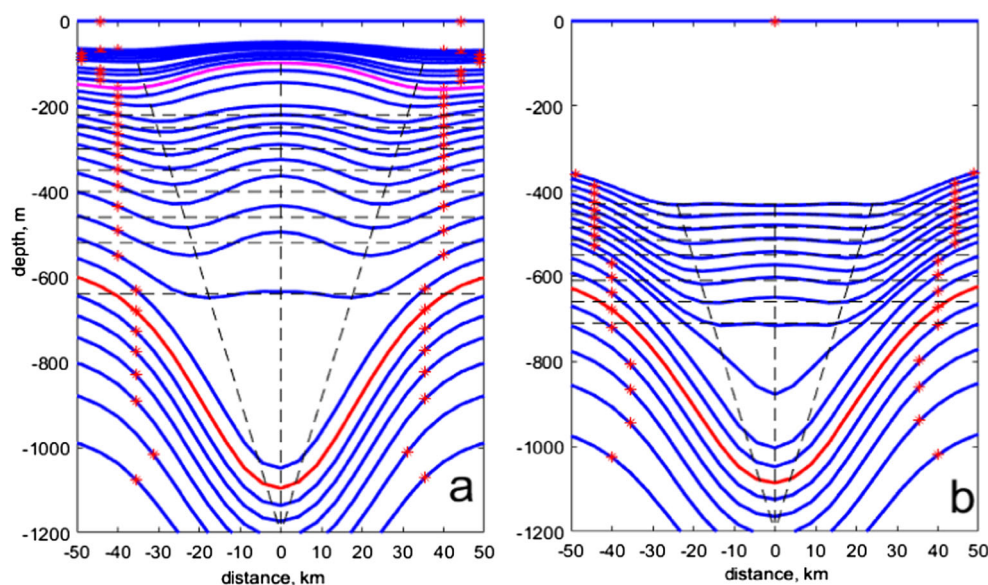
The maximum upward vertical velocity in the center of the LV core (the mid- and the upper ocean) is estimated to be  $V_o \sim 2 \times 10^{-3} \text{ cm s}^{-1}$ , while the maximum downward vertical velocity at 2500 m (deep ocean) is more than 3 times smaller:  $V_o \sim -0.6 \cdot 10^{-3} \text{ cm s}^{-1}$  (Fig. 4a).

The robustness of the mean vertical velocity pattern is confirmed by vertical sections of the mean isopycnal structure, derived from the MIT GCM simulations (Fig. 5). Averaged over the warm period (83% of the model time, Fig. 5a), as well as over the cold period, when deep convection reached the LV core, (17% of the model time, Fig. 5b), the isopycnals are shallowing along the eddy axis and deepening at the eddy periphery at least down to 600–700 m depth (see Bashmachnikov et al. 2017b for classification of the patterns). The bumps (depressions) in the depth of the isopycnal perfectly correspond to the locations where upward (downward) vertical velocities are observed (Fig. 4a). The isopycnals bend-downs converge towards the LV center with an increasing depth to finally form the downward bended isopycnals at the LV axis below 800 m depth. This is consistent with the convergence of the downward vertical flux below the LV core (Fig. 4a). Figure 5b demonstrates that the isopycnal pattern largely remains unchanged even during the episodes of deep convection in the upper part of the LV core. The maximum and the minima of the isopycnal depths remain at the same distance from the LV axis as they were during the warm season (Fig. 5a), but their amplitudes decrease. This suggests the same structure of an overall weaker vertical circulation in the LV during the episodes for deep convection.

By continuity, the vertical motions in an axisymmetric vortex are associated with radial convergence and divergence. The continuity equation for an axisymmetric ( $\frac{\partial V_{\phi}}{\partial \phi} = 0$ ) vortex in cylinder coordinates is written as:

$$\left[ \frac{V_r}{r} + \frac{\partial V_r}{\partial r} \right] + \frac{\partial V_z}{\partial z} = 0 \quad (1)$$

**Fig. 5** Mean isopycnal depths (blue lines) across the LV as a function of distance from the LV axis, presented for two typical configurations of isopycnals for: (a) warm season, (b) cold season (when deep convection in the LV core is detected). Red stars mark the distances, where relative vorticity changes sign. Magenta and red isopycnals mark the upper and the lower boundaries of the LV core, respectively. Horizontal dashed lines mark selected depth levels. Vertical and tilted dashed lines mark the local maximum and minima of the isopycnals depths in the LV core



The radial divergence (the term in square brackets of Eq. (1)), derived from MIT GCM, is presented in Fig. 4c. In the upper 1700 m layer, the radial divergence is observed. It clearly intensifies towards the LV center and towards the sea surface and decreases to zero in the vortex skirt (at  $r \sim r(\omega=0)$ ) and below 1700-m level. In accordance with Eq. (1), the divergence pattern is consistent with that of the vertical velocity (Fig. 4a).

The radial and the vertical velocities in the vortex are linked to ageostrophic effects in the vortex. In mesoscale eddies with a small Rossby number, the ratio of the radial velocity to the azimuthal one corresponds to the ratio of the ageostrophic to the geostrophic velocity components (Carton 2001; Barcelo-Llull et al. 2017). In MIT GCM, the LV Rossby number is 0.1–0.2 (Bashmachnikov et al. 2017b). As the simulated radial velocities in the LV (Fig. 4b) are an order of magnitude smaller than the azimuthal ones (Fig. 4a), we may expect the same ratio of the ageostrophic forces to the geostrophic ones. The ageostrophic effects in eddies are mainly related to the centrifugal and frictional forces (Carton 2001). From Fig. 4b, we note that the radial velocities reach maximum in the region, where the azimuthal velocities are at maximum. Therefore, the divergence in the vortex core may be generated by the centrifugal forces in the rotating flow. In fact, the ratio of the inertial (centrifugal) to the Coriolis force,  $\left[\frac{V_\phi^2}{r}\right]/[f V_\phi]$ , in the LV core is 0.2–0.3 (Fig. 4e). This is close to the ratio of the radial to the azimuthal velocities, and also typical for mesoscale vortices with low Rossby number (Carton 2001).

The maximum radial velocities (Fig. 4b) are confined to the inner boundary of the region of maximum shear stress (Fig. 4d), where the processes of the turbulent exchange across the boundary of the vortex are the most intensive. The horizontal velocity decay rate due to turbulent dissipation is one of the standard outputs of MIT GCM (Adcroft et al. 2018). In the upper core, the decay rate reaches maximum in the inner LV skirt (Fig. 4f), in-between the region of the maximum velocity and the maximum shear stress. The horizontal velocity dissipation rate strongly increases towards the sea surface. Along the LV axis, the strongest maximum of the decay rate underlies the LV faster rotating core at 800–1000 m depth. The very similar structure is obtained for the velocity dissipate rate from in situ microstructure measurements (Fer et al. 2018). Intensified towards the sea surface, both the inertial forces and the turbulent decay of momentum induce an increase of the radial divergence towards the sea surface, which results in the upward vertical velocities in the upper part of the LV core. The ratio of the turbulent decay to Coriolis force is around 0.02–0.04, an order of magnitude smaller than that of the centrifugal to the Coriolis forces (Fig. 4e). Thus, we can assume that the radial ageostrophic component of the current velocity is primarily associated with the centrifugal force. Traces of filaments, seen in the vertical

velocity just outside the LV dynamic radius (Fig. 3), may present signs of such divergence.

The divergence in the LV core is, sometimes, also associated with a local divergence of the Ekman fluxes, caused by perturbations of the wind field over a vortex (Gaube et al. 2013). The vertical velocity is estimated as (Gaube et al. 2013):

$$V_{0E} = -\frac{3C_d\rho_a|V_a|}{2\rho f}\bar{\omega}_z$$

here  $C_d$  is wind friction coefficient,  $\rho_a = 1.2 \text{ kg m}^{-3}$  is air density,  $\rho = 1030 \text{ kg m}^{-3}$  is density of water,  $f = 1.4 \cdot 10^{-4} \text{ c}^{-1}$  is Coriolis parameter,  $V_a$  is wind speed in the driving layer,  $\bar{\omega}_z$  mean relative vorticity of the vortex core. Taking  $\rho_a/\rho = 10^{-3}$ ,  $C_d = 10^{-3}$  (Bowden 1983) and  $V_a = 5 \text{ m s}^{-1}$  and  $\bar{\omega}_z = 3 \cdot 10^{-5} \text{ c}^{-1}$  in the upper part of the LV core, we get the corresponding vertical velocity:  $V_{0E} = 1.5 \cdot 10^{-4} \text{ cm s}^{-1}$ .  $V_{0E}$  is an order of magnitude smaller than observed in the center of the LV (Fig. 4a). Therefore, the effect of local Ekman divergence due to eddy induced wind variations over the LV can be neglected.

The registered downward motion below the central parts of the LV core (1500 m and below, Fig. 4a) may be associated with Ekman divergence of the anticyclonic flow in presence of bottom friction. The characteristic vertical velocity can be estimated as (Pedlosky 1987):

$$V_0 = C\bar{\omega}_z \tag{2}$$

where  $C = \sqrt{\frac{K_z}{2f}}$ ,  $K_z$  is the coefficient of vertical turbulent viscosity and  $\bar{\omega}_z$  is the mean relative vorticity at the bottom. For  $V_{\phi, \text{max}} \sim 10 \text{ cm s}^{-1}$ , we define  $K_z \sim 2.5 \cdot 10^{-3} V_{\phi} \sim 2.5 \cdot 10^{-4} \text{ m}^2 \text{ s}^{-1}$  (Bowden 1983), which is in the range of the values observed for the turbulent exchange in the bottom layer in the presence of mesoscale vortices (Ozmidov 1986; Siedler et al. 2001; Bashmachnikov et al. 2013b). Taking the average relative vorticity in the lower part of the LV (MIT GCM results)  $\bar{\omega}_z \sim -3 \cdot 10^{-6} \text{ s}^{-1}$ , we get  $V_0 \approx -0.5 \cdot 10^{-3} \text{ cm s}^{-1}$ .  $V_0$  is close to the vertical velocity registered at the bottommost levels of the model simulations (Fig. 4a). Thus, the bottom friction can cause the observed downward velocities in the lower part of the vortex.

### 3.3 Radial pattern of the vertical velocity from patterns of the eddy azimuthal velocity

An analysis of the experimental data of vortex dynamics suggests that the vorticity lines in the vortices are often not rectilinear but helical (Kuibin and Okulov 1996; Alekseenko et al. 1999). If we assume, that the vorticity lines can be approximated by canonical helical spirals, the azimuthal (circumferential) and the axial (vertical) velocity components in an axisymmetric

vortex can be linked for any particular radial distribution of relative vorticity (Kuibin and Okulov 1996). In this approach, the center of the radial distributions slides along the helical thread, along which the characteristics of the vortex do not change. Certainly being a simplification of the real vortices, this approach, however, allows us reducing the model dimensions from 3D to 2D. A detailed description of the theory of vortices with helical symmetry is given by Kuibin and Okulov (1996), Alekseenko et al. (1999, 2007).

Intense geophysical vortices in the atmosphere, like tornado, are often observed to the form the helical spirals. This phenomenon is dynamically linked to formation of vortex instabilities, forced by interaction of the vortices with other dynamic structures (Alekseenko et al. 2007). Contrary to the atmosphere, there are no direct observations of the helical structure of ocean vortices, but this can be explained by technical difficulties for deriving simultaneous detailed snapshots of their characteristics at various depth levels. However, observations of tilting of the axis of oceanic vortices (Walsh et al. 1997; Bashmachnikov et al. 2013a) suggest that at least some of them, similar to the atmospheric vortices, may hold the helical structure.

The application the theory of helical vortices to oceanic structures is developed by Belonenko et al. (2017), to which we refer reader for details. Here, we limit our description to the most important results of the theory. We consider the radial, the azimuthal and the vertical components of the velocity vector ( $V_r, V_\phi, V_z$ ) and of the relative vorticity vector ( $\omega_r, \omega_\phi, \omega_z$ ) in the system of the cylindrical coordinates ( $r, \phi, z$ ) centered at the vortex axis at any depth level. The axis is aligned with the thread of the peak relative vorticity of the vortex core. In the following theoretical estimates, we assume the radial velocity in the vortex core  $V_r=0$  everywhere, except for the uppermost and the lowermost parts of the vortex. Therefore, we assume the areas of fluid divergence all above and below the subsurface vortex core (in the near-surface and in the near-bottom layers), while the theoretical solutions will be limited to the intermediate depths, at the levels of the vortex core. This is a certain simplification, as it follows from our previous discussion (Section 3.2 and Fig. 4b, c); however, the intensification of the vortex divergence in the upper ocean and near the bottom justifies this approach. The two components of the velocity of an axisymmetric columnar vortex are (Kuibin and Okulov 1996):

$$\begin{aligned} V_\phi &= \frac{1}{r} \Phi(r) \\ V_z &= V_0 - \frac{1}{l} \Phi(r) \end{aligned} \tag{3}$$

where  $V_0$  is the axial vertical velocity ( $V_0 = V_z(r=0)$ ),  $h = 2\pi l$  is the vertical spacing between the helical lines of relative vorticity.

As

$$\omega_z = \frac{1}{r} \frac{\partial}{\partial r} (rV_\phi) \tag{4}$$

in view of Eq. (3), for an axisymmetric vortex, function  $\Phi(r)$  can be determined through the radial distribution of the relative vorticity ( $\omega_z$ ):

$$\Phi(r) = \int_0^r \omega_z(r') r' dr' \tag{5}$$

When the flow is barotropic, incompressible and non-viscous, the velocity field (3) satisfies the Euler's equations for any radial distribution of the relative vorticity. The continuity equation for the non-divergent ( $V_r=0$ ) axisymmetric ( $V_\phi=0$ ) core region of a vortex is written as:  $\frac{\partial V_z}{\partial z} = 0$ . Therefore, the dependence of the vertical velocity on  $z$  can be neglected. In view of Eq. (3), this equation is satisfied, in particular, for:

$$V_0(z) = const, \frac{\Phi(z)}{l(z)} = const \tag{6}$$

We apply Eq. (6), neglecting relatively small vertical variations of  $V_0$  in the LV core region, at 100–800 m depth (Fig. 4a). Further, consistent with observations (Section 3.2) and as it follows from the assumed non-divergent character of the flow, for any depth level in the selected depth range, the integral of the vertical velocity over any horizontal section of the vortex is assumed to be zero:

$$Q = 2\pi \int_0^{n\varepsilon} r' V_z dr' = 0 \tag{7}$$

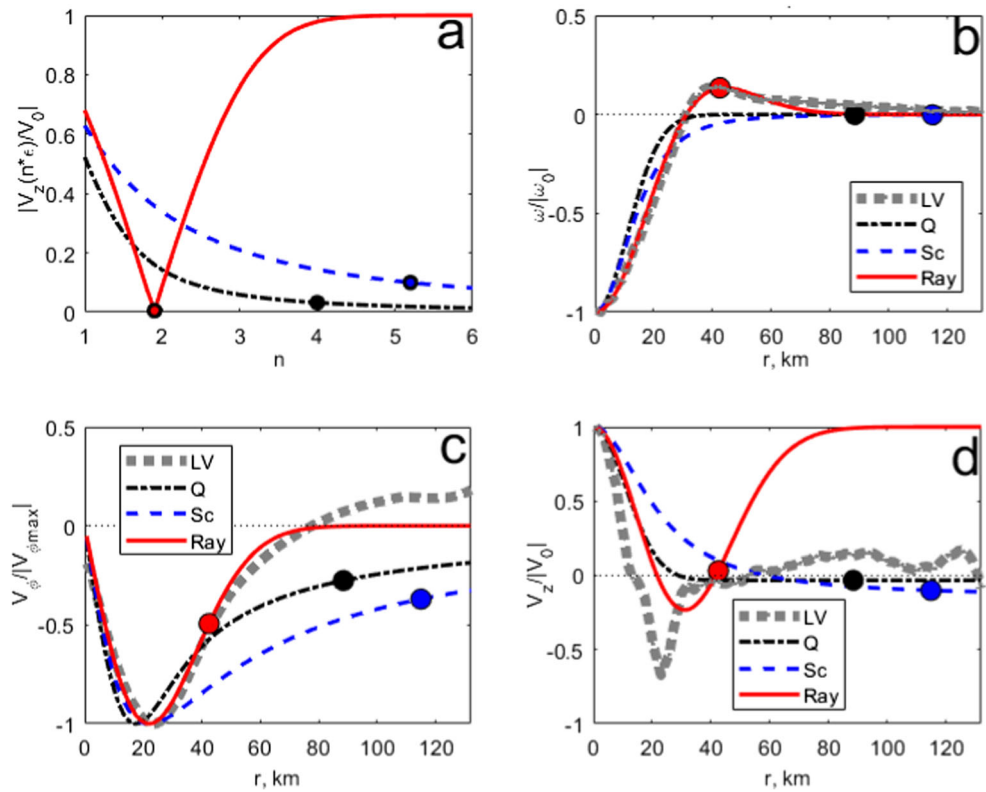
Here,  $\varepsilon$  is the vortex dynamic radius and  $n$  (not necessarily an integer) is taken, such that the distance  $n\varepsilon$  marks the limit of the valid solution. Naturally,  $n\varepsilon$  is expected to represent the vortex boundary, and, therefore, for any of theoretical continuous distributions of the relative vorticity in Eq. (4), at  $r \geq n\varepsilon$  we expect all the dynamic characteristics of the vortex to be significantly smaller than those in the vortex core. In particular, for the vertical velocity, the following condition should be true:

$$V_z(n\varepsilon)/V_0 \ll 1 \tag{8}$$

The solution of Eqs. (3–7) depends on a radial distribution of the relative vorticity ( $\omega_z$ ) in the vortex. In this paper, we present solutions for three commonly used radial distributions: Scully (1975), Rayleigh (Carton 2001; Bashmachnikov et al. 2015) and Q (Batchelor 1964).

For Scully vortex  $\omega_z = \frac{\Gamma}{\pi} \frac{\Gamma}{r}$ , where  $\Gamma=const$  is the vortex circulation. Applying Eqs. (7–8), we select the smallest  $n$ , such that  $V_z(n\varepsilon)$  is less than 10% of  $V_0(n)$  (Fig. 6a). This is

**Fig. 6** Normalized dynamic characteristics of the LV core (0–1000 m, gray dotted curves) and the theoretical results with  $\varepsilon=22$  km for Scully vortex (blue dashed curves), for Q-vortex (black dash-dotted curves) and for Rayleigh vortex (red solid curves): **(a)** the absolute value of the normalized vertical velocity  $|V_z(n\varepsilon)/V_0(n)|$  as function of  $n$ . The solution artificial cut off at  $r=n\varepsilon$  is marked with filled circles: for Scully vortex  $n=5.2$ , for Q-vortex  $n=4$  and for Rayleigh vortex  $n=1.9$ ; **(b)** radial pattern of the normalized relative vorticity; **(c)** radial pattern of the normalized azimuthal velocity and **(d)** radial pattern of the normalized vertical velocity. We consider the solutions only to the left of the corresponding cutoff points



satisfied for  $n=5.2$  (Belonenko et al. 2017), and the radial distribution of the vertical velocity is:

$$V_z(r) = V_0 \left( 1 - \frac{r^2}{0.877(r^2 + \varepsilon^2)} \right), \text{ where } V_0 = 0.4 \frac{\Gamma}{\pi l} \text{ and } r \leq 5.2\varepsilon \quad (9)$$

For Q-vortex, also known as the Batchelor vortex,  $\omega_z(r) = \frac{2\alpha\Gamma}{\pi} \exp(-\alpha r^2)$ . As in Bashmachnikov et al. (2017a), we take  $\alpha = \frac{1}{0.5\varepsilon^2}$ , so that the maximum azimuthal velocity of the Q-vortex is close to that of the Rayleigh vortex for the same  $\varepsilon$ .  $V_z(n\varepsilon)$  less than 1%  $V_0$  is reached already for  $n \geq 2.3$  (Fig. 6a). However, for such  $n$ , an azimuthal velocity at this distance from the vortex center is still over 50% of its maximum value. Therefore, we take  $n = 4$  as the breakpoint of the solution (Bashmachnikov et al. 2017a):

$$V_z = 1.032 \cdot V_0 [\exp(-2r^2/\varepsilon^2) - 0.031], \text{ where } V_0 = \frac{\Gamma}{\pi l} \text{ and } r \leq 4\varepsilon \quad (10)$$

For Rayleigh vortex,  $\omega_z(r) = \frac{\Gamma}{\pi\varepsilon^2} \left( 1 - \frac{r^2}{2\varepsilon^2} \right) \exp\left(-\frac{r^2}{2\varepsilon^2}\right)$ , the  $|V_z(n\varepsilon)/V_0|$  is below 1% is reached in a limited region with

minimum at  $n = 1.9$  (Fig. 6a). The resulting solution is (Belonenko et al. 2017):

$$V_z(r) = V_0 \left[ 1 - \frac{r^2}{0.6\varepsilon^2} \exp\left(-\frac{r^2}{2\varepsilon^2}\right) \right], \text{ where } V_0 = 0.3 \frac{\Gamma}{\pi l} \text{ and } r \leq 1.9\varepsilon \quad (11)$$

There are advantages and disadvantages in approximation of the time-averaged radial structure of different dynamic parameters of the LV with in Scully, Rayleigh and Q-vortices (Fig. 6b–d). For of Q-distribution, the radial characteristics decrease more rapidly with  $r$ , than for Scully-distribution, and better approximate the LV radial structure. Further, for a Scully vortex,  $V_0$  amplifies to infinity with increasing  $n$ . This is not the case for a Q-vortex. Nevertheless, all the radial distributions of the presented dynamic characteristics of the LV are better approximated by Rayleigh vortex (Fig. 6b–d). Only Rayleigh radial profiles allow a region of positive relative vorticity and of negative vertical velocity in the vortex skirt (Fig. 6b, d). However, the essential deficiency of using Rayleigh profile is that Eq. (8) is satisfied only in a very limited range of  $r$ -values (Fig. 6a), and we are forced to “cut off” the solution when the vortex azimuthal velocity and relative vorticity still show rather significant values (Fig. 6c). Radial profiles of all basic dynamic characteristics below the

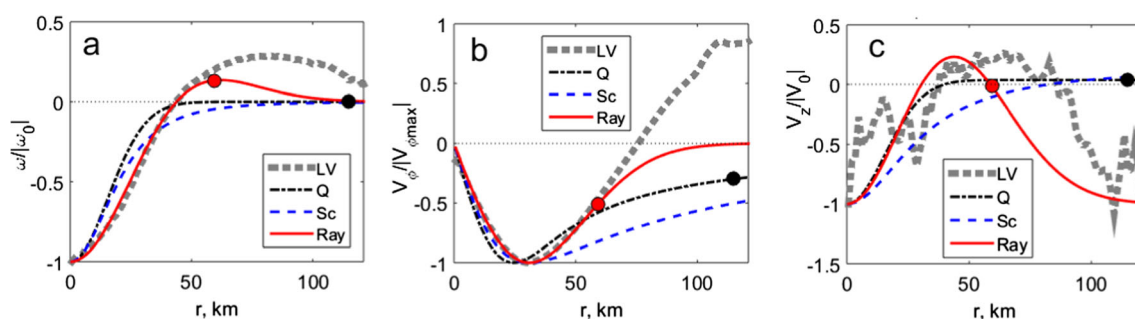


**Fig. 7** Normalized dynamic characteristics of the LV near the ocean bottom (1500–2500 m, gray dotted curves) and the theoretical results with  $\varepsilon=31$  km for Scully vortex (blue dashed curves), for Q-vortex (black dash-dotted curves) and for Rayleigh vortex (red solid curves). Radial

profiles of: (a) the normalized relative vorticity, (b) the normalized azimuthal velocity and (c) the normalized vertical velocity. Filled circles show the cutoff points for the selected  $n$ -values

LV core (Fig. 7) are also better approximated when using the Rayleigh profiles of relative vorticity, as compared to other radial distributions used here.

Since we do not consider the regions of the horizontal divergence in the theoretical solution, we cannot estimate the maximum vertical velocity along the vortex axis ( $V_0$ ). However, Eqs. (9–11) permit to conclude, that for the same dynamic radius and for the same maximum azimuthal velocity,  $V_0$  in Rayleigh vortex is 2.5–3 times higher than that for Scully or Q- vortices. The higher  $V_0$  is due to the downwards fluxes at the periphery of the vortex core in Rayleigh vortex under the assumption given by Eq. (7).

The results show stronger deviations of the mean velocity/vorticity pattern from the Rayleigh profile with distance from the LV center. A stronger cyclonic vorticity in MIT GCM simulations, compared to the theoretical Rayleigh profile, detected over 50–60 km distance from the LV center is due to an influence of two or three cyclonic vortices most of time surrounding the LV (Volkov et al. 2015). The presence of the cyclonic structures at the LV periphery may be a sign the LV energy decay via formation of ringlets (Nof 1993). These vortices distort the inherent dynamic properties in the outer skirt of the LV, adding to the deviation of the radial profiles from the theoretical ones (Figs. 6b–d and 7a–c).

## 4 Discussion and conclusions

In this paper, we investigate 3D structure of thermohaline and dynamic parameters of the quasi-persistent subsurface Lofoten vortex in the primitive equation MIT GCM. Previous studies (Kohl 2007; Raj et al. 2015; Volkov et al. 2015; Isachsen 2015; Bashmachnikov et al. 2017b) and our analysis show a close correspondence in the vertical and horizontal structure of the LV, compared to what is derived from in situ and satellite observations. In particular, we showed that the model adequately reproduces 3D structure of thermohaline and isopycnal anomalies in the LV. We have also shown that the derived

patterns of temperature, salinity and density anomalies in the vortex, as well as those of the radial velocity, are consistent with the model-derived time-averaged patterns of the vertical velocity. This confirms robustness of the mean vertical velocity field of the LV obtained from the MIT CGM simulations.

The results show that, when dynamic perturbations at the vortex boundary are removed, vertical velocity in the LV presents a rather complex pattern in  $z-r$  space, schematically presented in Fig. 8. This pattern reminds those of the secondary circulation in Taylor caps over the seamounts (Mullineaux and Mills 1997; White et al. 2007), but with some important differences. The secondary circulation is found to be forced by the two regions with a strong divergence: above the core (also, a weaker one, at the core level) and near the bottom. Only the

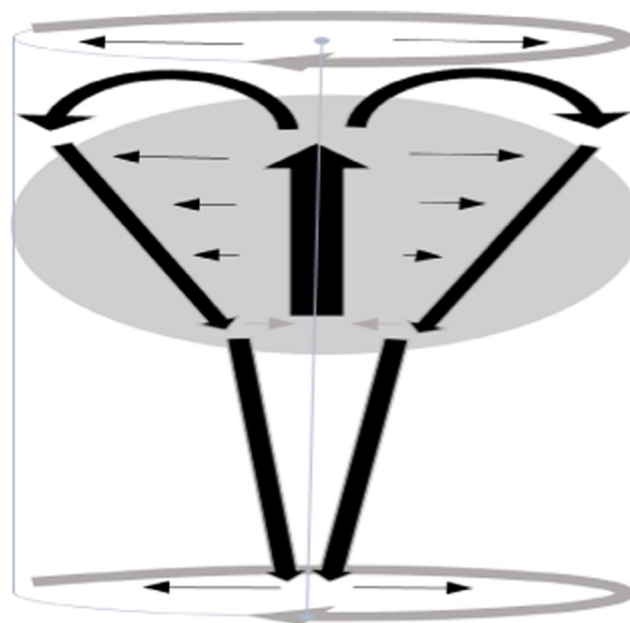


**Fig. 8** Schematics of the vertical and radial velocity structure in an anticyclonic vortex with a subsurface core. The gray area is the vortex core, the gray arrow represents the main anticyclonic circulation of the vortex, black arrows represent the secondary circulation in the vortex

second one is reported for Taylor caps (Lavelle 2006; White et al. 2007). Convergence of the maximum downward vertical velocity towards the vortex axis with increasing depth also is not observed in Taylor caps. Importantly, the upward vertical velocities in and above the core, coupled with the downward motions at the vortex periphery, increase the radial gradients of water density, thus maintaining the anticyclonic circulation against dissipation.

The mechanisms for maintaining the secondary pattern are also different from what has been suggested for Taylor caps (White et al. 2007). As in Taylor caps, the lower pattern of the secondary circulation in the anticyclonic vortex is forced by friction in the bottom Ekman layer (Pedlosky 1987). However, in the LV, the near-bottom divergence is found to be fed by a weak convergence of the downward flows at the vortex core periphery above. No ascending motions at the vortex periphery in the deep ocean were detected. In the upper part of the LV, the divergence is found to be forced mostly by the centrifugal force, while that due to the turbulent decay of the azimuthal velocity is found to be one order less (except in the uppermost ocean, where it may have a comparable effect). The importance of the inertial forces in ocean eddy dynamics has been highlighted in previous studies (see, for example, Carton 2001; Chelton et al. 2011). In this paper, we have demonstrated a link between the inertial force and the secondary circulation in the vortex. The wind forcing, suggested as one of the mechanisms for divergence in the upper parts of anticyclones (Gaube et al. 2013), is found to negligibly small for the LV.

The MIT GCM used in this study underestimates the peak azimuthal velocities in the LV, compared to in situ data (Søiland et al. 2016; Fer et al. 2018). Therefore, it underestimates the relative role of the centrifugal force. The turbulent dissipation of horizontal velocity in the model seems to be also underestimated, when compared with observations by Fer et al. (2018). Following our analysis, this suggests a higher peak vertical velocity in the LV core in the real ocean as compared to the estimates from MIT GCM.

Subsurface anticyclones are often characterized by negative SST anomalies over their cores (Bashmachnikov et al. 2013a; Ciani et al. 2015). It has been suggested that differential advection of the surrounding water into the core is the main reason for the observed negative SST anomalies over the anticyclonic Mediterranean water eddies (meddies) in the subtropical Atlantic (Bashmachnikov et al. 2013a). Negative temperature anomalies over the LV are associated with the secondary circulation in and above the LV core, which uplifts the isotherms above the core while water temperature decreases with depth (see, for example, Raj et al. 2015). The difference in the mechanisms may be related to difference in the core depths of the two types of eddies, as well as of a much lower  $f/N$  ratio in the subtropics than in the subpolar region (see Bashmachnikov et al. 2014; Ciani et al. 2015, 2017). Having cores at 600–1500 m, meddies do not directly

influence the strongly stratified subtropical upper ocean. The LV core is much shallower (200–1000 m) and the vortex induces the near-surface divergence and the associated rise of the isotherms.

The radial structure of the vertical velocity in the LV, derived from MIT GCM simulations, is further compared to the results of the theory of vortices with helical symmetry (Kuibin and Okulov 1996; Alekseenko et al. 1999, 2007). The theory (Eqs. 3–5) permits relating radial profiles of vertical velocity to those of the relative vorticity. Although the theoretical results use a strongly simplified vortex dynamic pattern by assuming divergence only above and below the core of an isolated vortex, Rayleigh vortex presents a fairly realistic approximation of the radial pattern of the vertical velocity. In particular, the theoretical results demonstrate that, since in MIT GCM the peak relative vorticity in the LV core is underestimated, the simulations should also underestimate the peak vertical velocity. Unfortunately, these conclusions are presently impossible to verify since no observations of the vertical velocity in the LV are available.

Further theoretical advances are required, including account for the vortex divergence, to allow the theoretical evaluation of the peak vertical velocity along the vortex axis. Extending the theory to account for the centrifugal force can allow estimating the vertical velocities in ocean eddies from observations of horizontal velocity patterns.

**Acknowledgements** The authors acknowledge support of Russian Science Foundation (RSF, project No. 18-17-00027). D. Volkov was supported by the NASA Physical Oceanography program (Grant NNX11AE27G) and by the base funds of NOAA Atlantic Oceanographic and Meteorological Laboratory.

## References

- Adcroft A, Campin JM, Dutkiewicz S, Evangelinos C, Ferreira D, Follows M, ..., Hill E (2018) MITgcm Documentation: 1–306
- Alekseenko SV, Kuibin PA, Okulov VL, Shtork SI (1999) Helical vortices in swirl flow. *J Fluid Mech* 382:195–243
- Alekseenko SV, Kuibin PA, Okulov VL (2007) Theory of concentrated vortices. An introduction. Springer, Berlin 506 p
- Alekseev GV, Bagryantsev MV, Bogorodskiy PV, Vasin VV, Shirokov PE (1991) Structure and circulation of water in the area of anticyclonic eddy in the northeastern Norwegian Sea [in Russian]. *Probl Arctic Antarct* 65:14–23
- Arbic BK, Scott RB, Chelton DB, Richman JG, Shriver JF (2012) Effects of stencil width on surface ocean geostrophic velocity and vorticity estimation from gridded satellite altimeter data. *J Geophys Res* 117: C03029, <https://doi.org/10.1029/2011JC007367>
- Barcelo-Llull B, Sangrà P, Pallàs-Sanz E, Barton ED, Estrada-Allis SN, Martínez-Marrero A et al (2017) Anatomy of a subtropical intrathermocline eddy. *Deep Sea Res I* 124:126–139
- Bashmachnikov IL (2017) Seasonal and interannual variability of the position of the dynamic and thermal fronts of the Barents, Norwegian and Greenland seas [in Russian]. Conference materials “The Seas of Russia: science, security, resources”, 3–7 October 2017: 29–30

- Bashmachnikov I, Boutov D, Dias J (2013a) Manifestation of two meddies in altimetry and sea-surface temperature. *Ocean Sci* 9(2): 249–259
- Bashmachnikov I, Loureiro C, Martins A (2013b) Topographically induced circulation patterns and mixing over condor seamount. *Deep Sea Res II* 98:38–51
- Bashmachnikov I, Carton X, Belonenko T (2014) Characteristics of surface signatures of Mediterranean water eddies. *J Geophys Res C119*: 1–22. <https://doi.org/10.1002/2014JC010244>
- Bashmachnikov I, Neves F, Calheiros T, Carton X (2015) Properties and pathways of Mediterranean water eddies in the Atlantic. *Prog Oceanogr* 137:149–172
- Bashmachnikov IL, Belonenko TV, Kuibin PA (2017a) The application of the theory of the columnar Q-vortex with helical structure to the description of the dynamic characteristics of the Lofoten vortex of the Norwegian sea [in Russian]. *Vestn St Petersburg Un-ta Ser.7* 62(3):221–336. <https://doi.org/10.21638/11701/spbu07.2017.301>
- Bashmachnikov IL, Sokolovskiy MA, Belonenko TV, Volkov DL, Isachsen PE, Carton X (2017b) On the vertical structure and stability of the Lofoten vortex in the Norwegian Sea. *Deep Sea Res I* 128:1–27. <https://doi.org/10.1016/j.dsr.2017.08.001>
- Batchelor GK (1964) Axial flow in trailing line vortices. *J Fluid Mech* 20: 645–658
- Belonenko TV, Volkov DL, Ozhigin VK, Norden YuE (2014) Circulation of waters in the Lofoten Basin of the Norwegian Sea, [in Russian]. *Vestn S. Petersbur. Un-ta, Ser.7. 2*:108–121
- Belonenko TV, Bashmachnikov IL, Koldunov AV, Kuibin PA (2017) On the vertical component of velocity in the Lofoten vortex of the Norwegian Sea [in Russian]. *Izvestiya Atmos Ocean Phys* 53(6): 641–649. <https://doi.org/10.1134/S0001433817060032>
- Bowden KF (1983) *Physical oceanography of coastal waters*. Ellis Horwood Limited, Chichester, p 302
- Capet A, Mason E, Rossi V, Troupin C, Faugère Y, Pujol I, Pascual A (2014) Implications of refined altimetry on estimates of mesoscale activity and eddy-driven offshore transport in the Eastern Boundary Upwelling Systems. *Geophys Res Lett* 41(21): 7602–7610
- Carton X (2001) Hydrodynamical modelling of oceanic vortices. *Surv Geophys* 22:179–263
- Chelton DB, Schlax MG, Samelson RM, de Szoeke RA (2007) Global observations of large oceanic eddies. *Geophys Res Lett* 34:L15606. <https://doi.org/10.1029/2007GL030812>
- Chelton DB, Schlax MG, Samelson RM (2011) Global observations of nonlinear mesoscale eddies. *Prog Oceanogr* 91:167–216
- Ciani D, Carton X, Bashmachnikov I, Chapron B, Perrot X (2015) Influence of deep vortices on the ocean surface, discontinuity, non-linearity, and complexity. 4(3):281–311. <https://doi.org/10.5890/DNC.2015.09.006>
- Ciani D, Carton X, Aguiar AB, Peliz A, Bashmachnikov I, Ienna F, Charron R, Santoleri R (2017) Surface signature of Mediterranean water eddies in a long-term high-resolution simulation. *Deep-Sea Res I Oceanogr Res Pap* 130:12–29
- Fer I, Bosse A, Ferron B, Bouruet-Aubertot P (2018) The dissipation of kinetic energy in the Lofoten Basin Eddy. *J Phys Oceanogr* 48(6): 1299–1316
- Gaube P, Chelton DB, Strutton PG, Behrenfeld MJ (2013) Satellite observations of chlorophyll, phytoplankton biomass, and Ekman pumping in nonlinear mesoscale eddies. *J Geophys Res C118*. <https://doi.org/10.1002/2013JC009027>
- Good SA, Martin MJ, Rayner NA (2013) EN4: Quality controlled ocean temperature and salinity profiles and monthly objective analyses with uncertainty estimates. *J Geophys Res Oceans* 118(12): 6704–6716
- Golivets SV, Koshlyakov MN (2003) Cyclonic vortices of the subantarctic front and formation of Antarctic intermediate water. *Oceanology [in Russian]* 43(3):325–338
- Hansen C, Kvaleberg E, Samuelsen A (2010) Anticyclonic eddies in the Norwegian Sea; their generation, evolution and impact on primary production. *Deep Sea Res I* 57(9):1079–1091
- Isachsen PE (2015) Baroclinic instability and the mesoscale eddy field around the Lofoten Basin. *J Geophys Res* 120(4):2884–2903
- Ivanov VV, Korablev AA (1995a) Formation and regeneration of the pycnocline lens in the Norwegian Sea, [in Russian]. *Russ Meteorol Hydrol* 9:62–69
- Ivanov VV, Korablev AA (1995b) Dynamics of pycnocline lens in the Norwegian sea, [in Russian]. *Russ Meteorol Hydrol* 10:55–62
- Klein P, Lapeyre G (2009) The oceanic vertical pump induced by mesoscale and submesoscale turbulence. *Annu Rev Mar Sci* 1:351–375
- Kohl A (2007) Generation and stability of a quasi-permanent vortex in the Lofoten Basin. *J Phys Oceanogr* 37:2637–2651
- Kuibin PA, Okulov VL (1996) One-dimensional solutions a flow with a helical symmetry. *Thermophys Aeromech* 4:297–301
- Lavelle JW (2006) Flow, hydrography, turbulent mixing, and dissipation at Fieberling Guyot examined with a primitive equation model. *J Geophys Res* 111:C07014. <https://doi.org/10.1029/2005JC003224>
- Lozier MS (2010) Destructing the conveyor belt. *Science* 328:1507–1511. <https://doi.org/10.1126/science.1189250>
- Luo D, Lu Y (2000) The influence of negative viscosity on wind-driven, barotropic ocean circulation in a subtropical basin. *J Phys Oceanogr* 30(5):916–932
- Mahdinia M, Hassanzadeh P, Marcus PS, Jiang CH (2016) Stability of 3D Gaussian vortices in rotating stratified Boussinesq flows: linear analysis. *J Fluid Mech* 824:97–134. <https://doi.org/10.1017/jfm.2017.303>
- Maze JP, Arhan M, Mercier H (1997) Volume budget of the eastern boundary layer off the Iberian Peninsula. *Deep Sea Res I* 44(9–10):1543–1574
- McGillicuddy DJ, Anderson LA, Bates NR, Bibby T, Buesseler KO, Carlson CA et al (2007) Eddy/wind interactions stimulate extraordinary mid-ocean plankton blooms. *Science* 316(5827):1021–1026
- Mullineaux LS, Mills S (1997) A test of the larval retention hypothesis in seamount-generated flows. *Deep Sea Res* 44:745–770
- Nguyen AT, Menemenlis D, Kwok R (2011) Arctic ice-ocean simulation with optimized model parameters: approach and assessment. *J Geophys Res* 116:C04025. <https://doi.org/10.1029/2010JC006573>
- Nof D (1993) Generation of ringlets. *Tellus A* 45(4):299–310
- Ozmidov RV (1986) Diffusion of an impurity in the ocean, [in Russian]. Leningrad, *Gidrometeoizdat*, 280 p
- Paldor N (1999) Linear instability of barotropic submesoscale coherent vortices observed in the ocean. *J Phys Oceanogr* 29(7):1442–1452
- Pedlosky J (1987) *Geophysical fluid dynamics*. Springer Verlag, 710 p
- Pereskokov AI (1999) On the physical nature of large-scale counter-cyclical cycle in the water column of the Norwegian Sea, [in Russian]. *Rep Acad Sci* 364(4):549–552
- Pilo GS, Oke PR, Coleman R, Rykova T, Ridgway K (2018) Patterns of vertical velocity induced by eddy distortion in an ocean model. *J Geophys Res Oceans* 123(3):2274–2292
- Raj RP, Chafik L, Nilsen JEØ, Eldevik T, Halo I (2015) The Lofoten vortex of the Nordic seas. *Deep-Sea Res I* 96:1–14
- Romantsev VA (1991) Large-scale structure and characteristics of the average circulation of the water, [in Russian]. *Probl Arctic Antarc* 65:75–97
- Scully MP (1975) Computation of helicopter rotor wake geometry and its influence on rotor harmonic airloads. Massachusetts Inst. of Technology, Publ. ARSL TR 152–1, Cambridge
- Siedler G, Church J, Gould J (eds) (2001) *Ocean circulation and climate: observing and modelling the global ocean*, International Geophysics Series. Academic Press, San Diego. 77, ISBN 0–12–641351–7. XIX, p 715
- Søiland H, Rossby T (2013) On the structure of the Lofoten Basin Eddy. *J Geophys Res Oceans* 118(9):4201–4212

- Søiland H, Chafik L, Rossby T (2016) On the long-term stability of the Lofoten Basin Eddy. *J Geophys Res Oceans* 121(7):4438–4449
- Vaillancourt RD, Marra J, Seki MP, Parsons ML, Bidigare RR (2003) Impact of a cyclonic eddy on phytoplankton community structure and photosynthetic competency in the subtropical North Pacific Ocean. *Deep Sea Res I* 50:829–847
- Volkov DL, Lee T, Fu LL (2008) Eddy-induced meridional heat transport in the ocean. *Geophys Res Lett* 35(20)
- Volkov DL, Belonenko TV, Foux VR (2013) Puzzling over the dynamics of the Lofoten Basin—a sub-Arctic hot spot of ocean variability. *Geophys Res Lett* 40(4):738–743. <https://doi.org/10.1002/grl.50126>
- Volkov DL, Kubryakov AA, Lumpkin R (2015) Formation and variability of the Lofoten basin vortex in a high-resolution ocean model. *Deep Sea Res I* 105:142–157. <https://doi.org/10.1016/j.dsr.2015.09.001>
- Walsh D, Richardson PL, Lynch J (1997) Observations of tilting meddies. *Oceanogr Lit Rev* 2(44):84
- White M, Bashmachnikov I, Aristegui J, Martins A (2007) Physical processes and seamount productivity. In: Pitcher TJ, Morato T, PJB H, Clark MR, Haggan N, Santos RS (eds) *Seamounts: ecology, conservation and management*. Fish and Aquatic Resources Series, Blackwell, Oxford, Chapter 4, pp 65–84
- Wunsch C, Ferrari R (2004) Vertical mixing, energy, and the general circulation of the oceans. *Annu Rev Fluid Mech* 36:281–314
- Yu LS, Bosse A, Fer I, Orvik KA, Bruvik EM, Hessevik I, Kvalsund K (2017) The Lofoten Basin eddy: three years of evolution as observed by Seagliders. *J Geophys Res Oceans* 122:6814–6834. <https://doi.org/10.1002/2017JC012982>
- Zhmur VV (2011) Mesoscale vortices of the ocean, [in Russian]. GEOS, Moscow, 384 p